Fuel Processing Technology 278 (2025) 108325

Contents lists available at ScienceDirect

Fuel Processing Technology

journal homepage: www.elsevier.com/locate/fuproc

Support effect in Ni-based catalysts for methane steam reforming: Role of MxOy-Al_2O_3 (M = Ni, Mg, Co) supports for enhanced catalyst stability

Yi Lin [a], Zaixing Wang [b], Lina Tang [c], Shi Jiang [a], Yu Guo [a,*], Xiaoqin Liu [a,*]

[a] State Key Laboratory of Materials-Oriented Chemical Engineering, College of Chemical Engineering, Nanjing Tech University, Nanjing, China
[b] Department of Applied Physics, The Hong Kong Polytechnic University, Hung Hom, Hong Kong, China
[c] Zhejiang Zheneng Technology & Environment Group Co., Ltd, Hangzhou, China

ARTICLE INFO

Keywords:
Support effect
Ni-based catalyst
Methane steam reforming
Stability

ABSTRACT

Ni-based catalysts supported on composite metal oxides (NiO-Al_2O_3, MgO-Al_2O_3, Co_3O_4-Al_2O_3) were synthesized via coprecipitation followed by Ni impregnation to investigate the influence of support composition on catalyst stability in methane steam reforming. Accelerated deactivation protocols (methane decomposition, high-temperature sintering, hydrothermal oxidation) revealed hydrothermal oxidation as the primary cause of irreversible deactivation. The 10Ni/NiAl catalyst (10 wt% Ni/10 wt% NiO-Al_2O_3) showed remarkable regenerability after 923 K hydrothermal treatment, fully restoring its activity. This was attributed to coexisting reduced Ni species and readily reducible NiO, facilitating rapid reactivation. Other catalysts formed thermally stable $NiAl_2O_4$, leading to permanent deactivation. Methane cracking at 973 K had negligible effect, and 10Ni/NiAl catalyst exhibited the lowest carbon deposition (17.02 %). Under extreme hydrogen purged at 1223 K, only the 10Ni/CoAl catalyst exhibited a minor activity decline. The superior stability of 10Ni/NiAl was attributed to an in situ-formed NiAl composite metal oxides during 973 K calcination, which effectively anchored Ni particles, suppressed sintering, and prevented extensive oxidation.

1. Introduction

Hydrogen is widely recognized as a clean and efficient energy carrier, possessing a high gravimetric energy density (~142 MJ/kg), and playing a pivotal role in the global transition toward sustainable and decarbonized energy systems [1–4]. Among hydrogen production technologies, methane steam reforming (MSR) dominates commercially due to its high hydrogen yield, process maturity, and favorable economics [2,5]. As a highly endothermic reaction, MSR operates optimally at 973–1173 K, making it particularly suitable for integration with high-temperature energy conversion devices.

With the rapid development of decentralized energy systems, particularly in residential and small-scale industrial applications, on-site hydrogen generation coupled with fuel cell power systems has attracted significant attention. A prominent example is Japan's ENE-Farm initiative, which deploys domestic-scale combined heat and power (CHP) systems fueled by natural gas [6]. These systems predominantly utilize proton exchange membrane fuel cells (PEMFCs) owing to their compact design, low operating temperatures (333–353 K), high power density, and fast transient response [7,8]. In addition, high-temperature PEMFCs (HT-PEMFCs), operating at 393–473 K with phosphoric acid-doped polybenzimidazole (PBI) membranes, have been developed to enhance thermal integration and improve CO tolerance [9,10]. Nevertheless, even HT-PEMFCs suffer from thermal mismatch with MSR, requiring complex heat management and stringent gas purification to satisfy strict fuel purity requirements.

In contrast, solid oxide fuel cells (SOFCs), operating at 873–1273 K, provide direct thermal compatibility with MSR [11,12]. This thermal synergy enables internal reforming, streamlines heat integration, and improves overall system efficiency. Moreover, SOFCs exhibit broad fuel flexibility and strong tolerance to CO and unconverted hydrocarbons, making them particularly attractive for integrated reforming–fuel cell systems. Owing to these attributes, MSR–SOFC configurations have emerged as a promising pathway for high-efficiency, low-emission distributed power generation.

However, applying MSR in decentralized systems presents challenges distinct from those encountered in conventional large-scale operations. Industrial MSR reactors, such as those used in ammonia production, typically operate under high pressures (20–40 bar), low gas hourly space velocities (GHSV < 10,000 h^{-1}), and steady-state conditions [13]. In

* Corresponding authors.
E-mail addresses: mguoyu@njtech.edu.cn (Y. Guo), liuxq@njtech.edu.cn (X. Liu).

https://doi.org/10.1016/j.fuproc.2025.108325
Received 16 July 2025; Received in revised form 29 August 2025; Accepted 31 August 2025
Available online 8 September 2025

contrast, distributed systems demand low or atmospheric pressure, high GHSV ($>$ 10,000 h^{-1}), intermediate temperatures (873–1023 K), and frequent start-up/shut-down cycles. These stringent conditions impose severe demands on catalyst activity, structural stability, sintering resistance, and redox durability [14].

To address these challenges, the development of reforming catalysts specifically tailored for the dynamic and harsh operating conditions characteristic of MSR–SOFC systems is essential. Ni-based catalysts have received extensive attention due to their cost-effectiveness, high intrinsic activity, and well-established role in MSR. However, their practical application in decentralized systems remains limited by their vulnerability to deactivation and insufficient regenerability, defined as the ability to recover activity after operational cycles [15]. Although Ni effectively activates C—H bonds [16], it remains prone to sintering, coking, and steam oxidation under MSR conditions. The endothermic nature of MSR requires elevated temperatures for efficient reforming, particularly at high space velocities, which accelerate Ni particle agglomeration and coke formation. Ultimately leading to pore blockage and progressive loss of active sites [17–19]. Moreover, exposure to steam at temperatures above 973 K can lead to hydrothermal oxidation, a process that not only oxidizes metallic Ni but can also promote the formation of inert $NiAl_2O_4$ spinel, irreversibly disrupting the catalytic cycle and depleting active Ni^0 sites [20,21].

The support effect is critical in this context, and γ-Al$_2$O is commonly used as a support due to its high surface area and thermal stability, and can generate a strong metal-support interaction (MSI), which improves Ni dispersion and durability by anchoring the nanoparticles against sintering [22,23]. However, the strong interaction between NiO and Al_2O_3 may lead to the formation of $NiAl_2O_4$ spinel phases, significantly reducing the availability of active Ni^0 sites [24,25]. To overcome these limitations, recent studies have increasingly focused on composite metal oxide supports that offer enhanced structural stability and tunable basicity.

Composite oxides such as MgO-Al_2O_3 and Co_3O_4-Al_2O_3 have demonstrated superior performance compared to single oxides, primarily due to improved metal dispersion and optimized strong MSI [26]. Ni-Mg-Al catalysts prepared via coprecipitation–impregnation exhibit enhanced reducibility, superior Ni dispersion, and improved resistance to sintering under MSR conditions [16]. Likewise, Co-modified systems stabilize Ni nanoparticle via $CoAl_2O_4$ spinel formation, suppress coke formation, and extend long-term performance during hydrocarbon reforming [27]. The inclusion of MgO also increases the surface basicity, facilitating CO_2 adsorption and coke suppression [28].

Despite the widespread application of Ni-based composite catalysts, the role of Ni as a structural component in the support matrix remains insufficiently explored. While $NiAl_2O_4$ spinel structures have shown promise in dry reforming of methane (DRM), their synthesis typically requires high calcination temperatures ($\geq$ 973 K) and precise compositional control, complicating large-scale preparation [29]. In $MgAl_2O_4$-supported catalysts, the structural contribution of $MgAl_2O_4$ tends to be emphasized over the synergistic effects involving Ni [30]. Nevertheless, $NiAl_2O_4$-based catalysts have demonstrated superior performance in glycerol steam reforming and DRM compared to their Mg- and Co-based counterparts, benefiting from their optimal acidity, structural stability, and Ni—Al synergy, which are beneficial for Ni^0 stabilization and carbon suppression [31].

Although substantial progress has been made, the fundamental deactivation mechanisms of Ni-based composite catalysts remain insufficiently understood. While coke formation and sintering are recognized as primary deactivation pathways [32], the influence of support structures and steam-induced deactivation under realistic operating conditions requires further elucidation. For example, the exceptional coking resistance of Ni/$MgAl_2O_4$ in DRM suggests that spinel stability may play a crucial role in maintaining long-term activity, yet this correlation is not fully characterized [29].

While composite metal oxides significantly enhance the performance of Ni-based catalysts, research efforts remain uneven. Recent studies have made significant strides in developing coke- and sintering-resistant catalysts through various strategies [33–40]. However, a comprehensive understanding of catalyst stability under severe hydrothermal conditions and sequential multi-stress tests (coking, steaming, and sintering) is lacking. Furthermore, the role of Ni not just as the active phase but as an integral structural component of the support itself represents an innovative but less-explored strategy for achieving ultimate stability [31]. Addressing this scarcity of mechanistic studies on deactivation mechanisms will facilitate the rational design of robust catalysts for industrial applications. Given the frequent start-up and shut-down cycles inherent to integrated reforming–fuel cell systems, investigations into key deactivation factors and mitigation strategies are essential.

To bridge these gaps, the present study systematically investigates the influence of composite oxide supports on Ni-based catalyst performance under MSR conditions tailored for SOFC integration. A series of composite metal oxide catalysts, as 10Ni/NiAl (10 wt% Ni/10 wt% NiO-Al_2O_3), 10Ni/MgAl (10 wt% Ni/10 wt% MgO-Al_2O_3), and 10Ni/CoAl (10 wt% Ni/10 wt% Co_3O_4-Al_2O_3), were synthesized by modifying γ-Al_2O_3 with Ni, Mg, and Co. For comparison, two additional catalysts, 10Ni/Al (10 wt% Ni/Al_2O_3) and 20Ni/Al (20 wt% Ni/Al_2O_3), were prepared using γ-Al_2O_3 as the support. This study aims to systematically evaluate the influence of support effects on catalyst activity and stability in MSR and to identify the key factors governing deactivation. To comprehensively assess catalyst robustness, three targeted deactivation protocols were designed: forced coke deposition by methane decomposition, forced sintering at high temperature, and steam-induced deactivation. Additionally, the long-term stability of the most efficient catalyst was evaluated, along with the influence of start-up and shut-down cycles on its catalytic performance.

2. Experimental

2.1. Materials

The chemical reagents used in the experiment included Ni$(NO_3)_2{\cdot}6H_2O$, Mg$(NO_3)_2{\cdot}6H_2O$, Co$(NO_3)_2{\cdot}6H_2O$ and $NH_3{\cdot}H_2O$, which were purchased from Sinopharm Chemical Reagent Co., Ltd. γ-Al_2O_3 was obtained from Shanghai Aladdin Biochemical Technology Co., Ltd. All the chemicals were analytic grade and could be used directly without pretreatment.

2.2. Preparation of the catalysts

Aqueous solutions were prepared by dissolving the corresponding metal nitrates (Ni$(NO_3)_2{\cdot}6H_2O$, Mg$(NO_3)_2{\cdot}6H_2O$, Co$(NO_3)_2{\cdot}6H_2O$) in deionized water. A precise amount of γ-Al_2O_3 was then introduced to maintain a metal content of 10 %. Ammonia was added three times during stirring as a precipitant, with the objective of controlling the pH at 9. The mixture was then aged for 6 h, after which it was dried using a water bath at a temperature of 353 K. The material was further dried overnight at 383 K, and finally calcined in air at 973 K for 3 h, resulting in the formation of the various composite metal oxide supports.

To obtain different Ni-based catalysts, a secondary impregnation process was performed using 10 wt% Ni loaded on various composite metal oxide supports, utilizing Ni$(NO_3)_2{\cdot}6H_2O$ as the Ni precursor. The samples were first dried in a 353 K water bath, followed by overnight drying in an oven at 383 K. However, the calcination temperature was adjusted to 773 K, and the calcination time was once again set at 3 h.

For comparison, two baseline catalysts, 10Ni/Al and 20Ni/Al, were prepared using a conventional one-step impregnation method directly onto the γ-Al_2O_3 support, followed by calcination at 773 K for 3 h. This approach was deliberately chosen to create catalysts with a relatively weak MSI, which serves as a benchmark against which to evaluate the catalysts prepared on the co-precipitated composite supports. The co-precipitation method, in contrast, is designed to foster strong MSI by

integrating metal cations into the support lattice. This comparative experimental design is fundamental to isolating and understanding the "support effect" on catalyst stability and performance. The calcination temperature of 773 K was selected to ensure complete precursor decomposition without inducing excessive spinel formation in the baseline samples.

2.3. Catalyst characterization and catalytic performance evaluation

The experimental methodologies for catalyst characterization and activity testing (including accelerated deactivation experiments) are detailed in the Supporting Information.

3. Results and discussion

Before presenting the detailed catalytic results, it is crucial to highlight the intentional design strategy underpinning the synthesis of our catalysts, which leverages the distinct outcomes of co-precipitation and impregnation methods. The composite supports (NiAl, MgAl, CoAl) were prepared via co-precipitation to create atomically-mixed, homogeneous oxide structures. This method ensures that the promoter cations are structurally integrated into the alumina lattice, forming robust spinel-type phases that serve as stable anchors and generate beneficial surface defects.

Subsequently, the primary active Ni phase was introduced onto these pre-formed supports via impregnation. This second step deposits NiO nanoparticles onto the support surface, ensuring they are highly accessible and readily reducible to the active metallic Ni^0 state. The superior performance of the 10Ni/NiAl catalyst, as will be demonstrated, stems directly from this synergistic, two-step approach. It combines a stable, co-precipitated anchor with a highly active, impregnated surface phase, a design fundamentally different from the conventional single-step impregnation used for the 10Ni/Al control catalyst. This methodological distinction is key to understanding the structure-performance relationships discussed below.

3.1. MSR with different WHSV

Fig. 1 illustrates the time-on-stream performance of various Ni-based catalysts for MSR under different WHSV: F/W = 120,000 mL/(h·g_{cat}) (a) and 240,000 mL/(h·g_{cat}) (b). All tests were conducted at 973 K with a steam-to-carbon ratio (S/C) of 3. Among them, Cat-1 and Cat-2 represent commercially available catalysts. As shown in Fig. 1(a), all catalysts initially exhibit methane conversion rates exceeding 95 %. However, with prolonged reaction time, the activity of most catalysts decreases significantly, with the exception of 10Ni/NiAl, Cat-2 and 20Ni/Al. The ranking of catalyst activity based on the methane conversion rate after 20 h of reaction can be summarized as follows: Cat-1 < 10Ni/MgAl < 10Ni/Al < 10Ni/CoAl ≈ 20Ni/Al ≈ Cat-2 ≈ 10Ni/NiAl. When the F/W is increased to 240,000 mL/(h·g_{cat}), only 10Ni/NiAl maintains high activity and stability, while other catalysts demonstrate varying degrees of deactivation. Notably, Cat-1 undergoes complete deactivation after approximately 7 h of reaction. Although Cat-2 exhibits good initial stability within the first 10 h, a gradual decline in performance is observed thereafter, with an accelerated deactivation rate over time, as illustrated in Fig. 1(b).

These results demonstrate that current commercial catalysts fail to meet the long-term stability requirements under high-WHSV steam reforming conditions. Moreover, they highlight the importance of evaluating catalyst performance under realistic and demanding reaction environments when developing or selecting catalysts for practical applications.

3.2. XRD of the fresh and reduced catalysts

The XRD patterns in Fig. 2(a) reveal the evolution of the crystalline structure of NiAl samples with calcination temperature. All samples display characteristic diffraction peaks of γ-Al_2O_3 at 31.9°, 37.6°, 39.5°, 45.9°, 60.9°, and 67.0° (JCPDS No. 10–0425), indicating that the γ-Al_2O_3 crystalline structure remains stable throughout the different synthesis processes without significant phase transformation [22].

For the NiAl-773 sample, distinct diffraction peaks are observed at 43.3° and 62.9°, which are unambiguously assigned to the crystalline NiO phase (JCPDS No. 04–0835) [22]. Although the peak near 37.2° overlaps with that of Al_2O_3, the relatively higher intensity compared to pure Al_2O_3 suggests the presence of a superimposed contribution from NiO, implying a co-existence of both phases at this diffraction position.

Upon increasing the calcination temperature to 973 K (NiAl-973), the intensity of the NiO-related peaks at 43.3° and 62.9° diminishes significantly, with only a weak but discernible peak remaining at 43.3°. Nevertheless, the intensity of the 37.2° peak remains significantly more intense than that of pure γ-Al_2O_3. When the temperature is further raised to 1173 K (NiAl-1173), the 43.3° peak completely disappears, while the 37.2° peak still maintains elevated intensity. These results suggest that a solid-state reaction between NiO and Al_2O_3 to form a nickel aluminate spinel, $NiAl_2O_4$ (JCPDS No. 10–0339) [22,41,42].

Direct confirmation of the $NiAl_2O_4$ phase is challenging due to the severe overlap of its major diffraction peaks with those of γ-Al_2O_3. However, compelling evidence is provided by the systematic shift of the most intense γ-Al_2O_3 peak, as highlighted in the magnified view in Fig. 2 (b). The peak at 67.0° for pure γ-Al_2O_3 progressively shifts to a lower 2θ value of 66.4° for NiAl-1173. This shift is consistent with the incorporation of Ni^{2+} into the alumina lattice, forming the $NiAl_2O_4$ spinel, whose corresponding diffraction peak is located at approximately 65.5°. This observation provides strong evidence for the formation of a solid solution or spinel phase.

Following the secondary Ni loading (10Ni/NiAl), the intensity of the NiO peaks at 43.3° and 62.9° increases markedly compared to those of

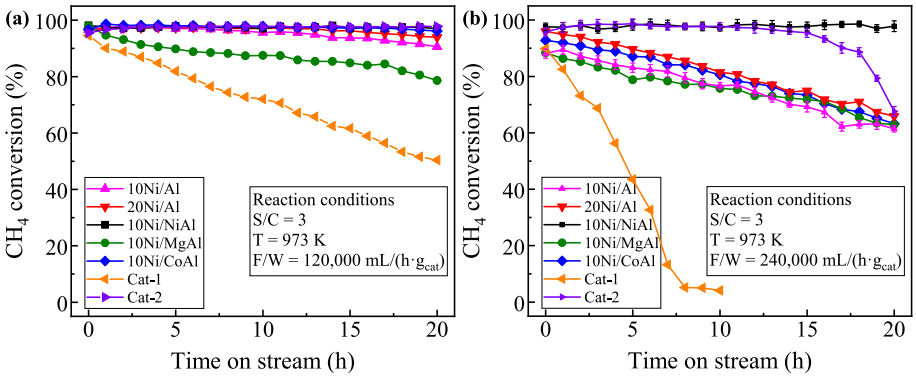

Fig. 1. Methane conversion stability of the prepared catalysts at two different WHSVs: (a) 120,000 mL/(h·g_{cat}) and (b) 240,000 mL/(h·g_{cat}).

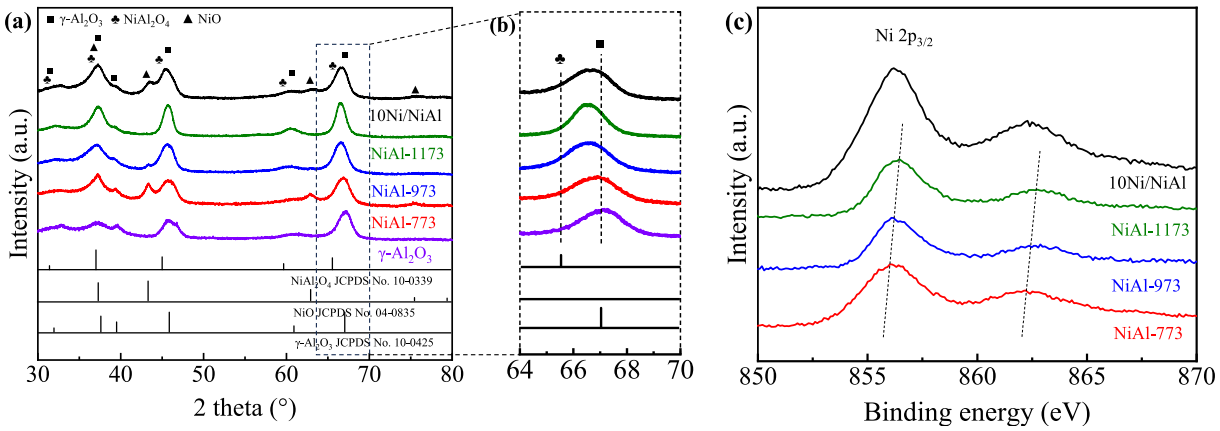

Fig. 2. Characterization of the NiAl-X composite supports calcined at different temperatures. (a) XRD patterns. (b) Magnified view of the γ-Al_2O_3 (440) peak region. (c) High-resolution Ni $2p_{3/2}$ XPS spectra.

the NiAl-973 support, suggesting that the impregnated Ni predominantly exists in the form of surface-dispersed NiO.

Fig. 2(c) shows the Ni 2p XPS spectra of NiAl-X samples. The Ni $2p_{3/2}$ peak for NiAl-773 observed at 855.5 eV signifies the presence of Ni^{2+} species resulting from the coexistence of NiO and $NiAl_2O_4$. Specifically, the peak at 854.6 eV corresponds to NiO species interacting with the support, while the peak at 856.5 eV is attributed to Ni^{2+} ions within the $NiAl_2O_4$ single crystal phase [22]. The binding energy gradually increases from 855.5 eV at 773 K to 856.1 eV at 973 K and further to 856.3 eV at 1173 K, accompanied by a gradual decrease in peak intensity as the calcination temperature rises. This trend indicates a stronger metal-support interaction and the partial integration of nickel into the Al_2O_3 lattice.

Collectively, the combined XRD and XPS analyses confirm that the thermal treatment significantly affects the Ni phase distribution, with higher calcination temperatures favoring the formation of stable $NiAl_2O_4$ spinel, which can potentially affect catalytic activity and stability during reforming reactions.

Fig. 3 presents the comparative XRD patterns of the fresh (a) and reduced (b) Ni-based catalysts, along with the H_2-TPR profiles of the fresh samples. Both the fresh and reduced catalysts retain the γ-Al_2O_3 structure, indicating that neither the preparation procedures nor the employed reduction conditions cause significant changes to the catalyst's crystalline framework.

Fig. 3(a) shows the XRD patterns of the freshly prepared catalysts. Compared with γ-Al_2O_3, the XRD patterns of the 10Ni/NiAl catalyst exhibit similar diffraction features, suggesting minimal structural alteration upon Ni incorporation. However, the 10Ni/MgAl and 10Ni/CoAl catalysts display more pronounced peak shifts toward lower angles at approximately 45° and 67°, which can be attributed to the characteristic reflections of spinel-type $MgAl_2O_4$ (JCPDS No. 77–1203) at 44.8° and 65.2°, and $CoAl_2O_4$ (JCPDS No. 44–0160) at 44.7° and 65.0°, respectively. Moreover, the diffraction peaks of $CoAl_2O_4$ and Co_3O_4 (JCPDS No. 43–1003) are known to be nearly indistinguishable, in agreement with previous studies [23,27,43].

The presence of characteristic $NiAl_2O_4$ peaks in the fresh 10Ni/Al and 20Ni/Al catalysts suggests the formation of a spinel phase even at the relatively low calcination temperature of 773 K [29]. To provide direct, microstructural evidence for this intriguing finding, HRTEM was performed on the 10Ni/Al sample. As shown in Fig. S2, the HRTEM images clearly reveal the presence of highly crystalline nanodomains at the Ni/support interface. The measured lattice fringe spacing of 0.242 nm is in excellent agreement with the (311) plane of the cubic $NiAl_2O_4$ spinel structure [44]. This unequivocally confirms that a well-crystallized $NiAl_2O_4$ phase is indeed formed during calcination at 773 K, a result of the strong interaction between the impregnated nickel species and the alumina support.

All catalysts display distinctive diffraction peaks attributed to NiO (JCPDS 04–0835) at 2θ angles of 37.3°, 43.3°, 62.9° and 75.4°.This observation highlights that NiO was generated on the support surface during the catalyst preparation process. A comparison between the 20Ni/Al and 10Ni/Al fresh catalysts reveals that the intensity of NiO characteristic peaks is significantly enhanced in 20Ni/Al, consistent with its higher Ni loading.

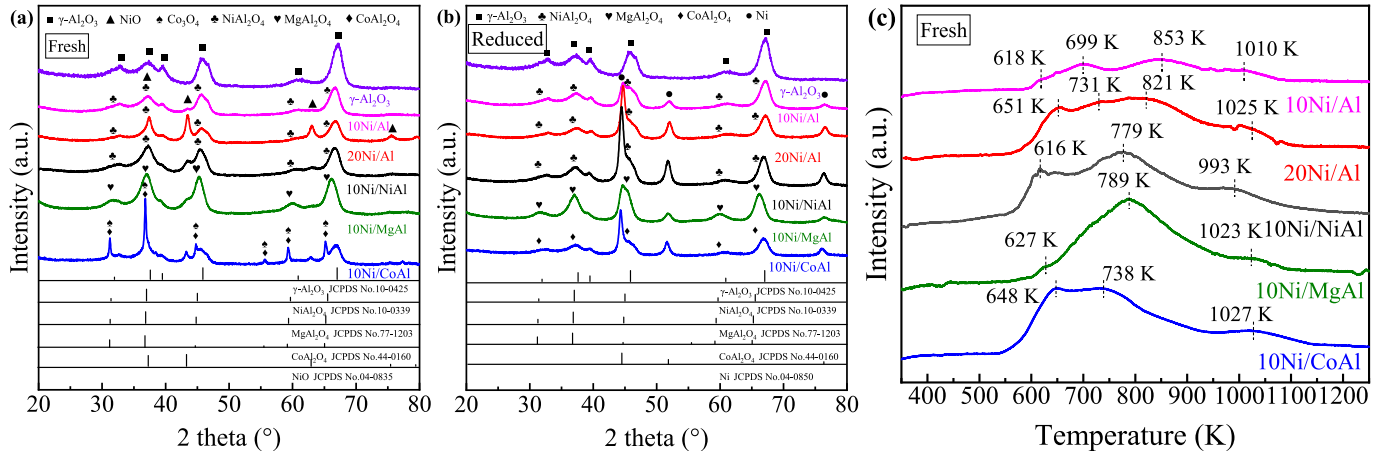

Fig. 3. Characterization of the Ni-based catalysts. (a) XRD patterns of fresh catalysts. (b) XRD patterns after reduction at 973 K. (c) H_2-TPR profiles.

Among these catalysts, the NiO peaks at 43.3° and 62.9° for 10Ni/MgAl appear broader and lower in intensity, indicating that the Ni particles on the catalyst are smaller and more evenly dispersed. Uskov et al. [45] reported that Ni-MgO-Al_2O_3 catalysts exhibit comparable activity to industrial methanation catalysts, attributing the enhanced dispersion of Ni to Ni-MgO interactions. Similarly, Braga et al. [46] demonstrated that Co doping in Ni-based catalysts modifies metal particle size and properties, enhancing the thermal stability of both Co and Ni oxides. Many other studies have also confirmed that bimetallic or polymetallic Ni-based catalysts can effectively improve Ni dispersion [47–49]. Similar results were also confirmed by the TEM morphologies and elemental distribution analysis, as shown in Fig. S3.

Fig. 3(b) exhibits that all catalysts retained their crystalline phases, even after reduction treatment at 973 K. In particular, the crystalline phases of spinel such as $NiAl_2O_4$, $MgAl_2O_4$ and $CoAl_2O_4$ remained intact with no evidence of crystal structure collapse. This observation suggests that the reduction temperature applied was insufficient to effectively reduce the spinel phases.

Compared with Fig. 3(a), the characteristic peaks of NiO at 43.3°, 62.8° and 75.4° have disappeared after reduction, while new diffraction peaks corresponding to Ni^0 (JCPDS 04–0850) emerged at 44.5°, 51.9° and 76.4° in Fig. 3(b), and these results confirm that the nickel oxide species on the fresh catalysts are reduced to metallic Ni after hydrogen reduction at 973 K [22,41]. Furthermore, neither nickel impregnation calcination, nor reduction processes caused detectable damage to the structural integrity of the catalyst support [31].

As the metallic state of Ni acts as the active center for MSR, pre-reduction of the catalyst is essential to ensure optimum performance. The H_2-TPR profiles shown in Fig. 3(c) provide valuable insights into the reduction behavior of the fresh catalysts, revealing hydrogen consumption over the temperature range of 373–1273 K, indicative of multiple reduction steps.

According to previous studies [29,32], three characteristic reduction peaks are typically observed NiAl-based catalysts in this temperature range. These peaks correspond to different degrees of interaction between NiO species and the alumina support. The first peak, occurring below 673 K, is assigned to the reduction of surface-exposed, weakly bound NiO species, which are more readily accessible and reducible. The second peak, ranging from 673 K to 873 K, is associated with the reduction of NiO species more strongly interacting with the support, resembling the reduction behavior of bulk NiO. In contrast, the third peak observed above 973 K corresponds to the reduction of stoichiometric nickel aluminum spinel ($NiAl_2O_4$), which is highly stable due to the strong Ni-Al_2O_3 interaction, and thus requires substantially higher temperatures for reduction [29].

As shown in Fig. 3(c), the reduction peaks in the low and medium temperature regions of 10Ni/NiAl, 10Ni/MgAl and 10Ni/CoAl should be attributed to the reduction of the oxide species of nickel, as these temperatures correspond to the typical reduction ranges for NiO. Specifically, for 10Ni/NiAl, the reduction peak observed at approximately 993 K is attributed to the reduction of $NiAl_2O_4$: $NiAl_2O_4(s) + H_2(g) \longleftrightarrow Ni(s) + Al_2O_3(s) + H_2O(g)$ [22]. This result confirms that the presence of $NiAl_2O_4$ in this catalyst, whose reduction at higher temperatures aligns with its intrinsic stability and strong metal–support interaction. For the 10Ni/MgAl catalyst, the observed high-temperature peaks are also likely due to the reduction of $NiAl_2O_4$ phases, since MgO itself is typically non-reducible under these conditions. Meanwhile, in the 10Ni/CoAl catalyst, the high-temperature reduction features can be attributed to the presence of both $CoAl_2O_4$ and $NiAl_2O_4$ spinel structures.

High-temperature reduction peaks assigned to $NiAl_2O_4$ are also detected in the 10Ni/Al and 20Ni/Al samples, corroborating the XRD analysis shown in Fig. 3(a). Compared with the 10Ni/NiAl sample, the reduction peaks in the low and medium temperature regions for the 10Ni/Al and 20Ni/Al samples shift to higher temperatures. This shift suggests that some of the nickel oxide species in the 10Ni/NiAl catalyst, especially those introduced during secondary nickel loading, exhibit higher dispersion and are therefore more readily reducible, reflecting improved metal dispersion due to the NiAl composite support.

To gain deeper insight into the metal-support interactions and their consequences, a detailed XPS analysis was conducted. The Ni $2p_{3/2}$ spectra (Fig. S4) reveal that the 10Ni/NiAl catalyst exhibits a Ni $2p_{3/2}$ peak at a higher binding energy compared to the 10Ni/Al reference. This positive shift signifies a strong MSI, where electron density is withdrawn from the Ni species by the underlying NiAl composite support. This electron-deficient state not only provides a strong anchoring effect to inhibit sintering but also increases the energy barrier for reduction, which perfectly explains the shift of the main reduction peaks to higher temperatures in its H_2-TPR profile.

Furthermore, analysis of the O 1s spectra (Fig. S5) provided a direct link between the support composition and its surface defect chemistry [2]. Deconvolution of the O 1s peaks revealed a distinct hierarchy in the concentration of surface defect oxygen, which followed the clear order (Table S1): 10Ni/NiAl > 10Ni/MgAl > 10Ni/CoAl. This trend is consistent with established principles of charge compensation [50], where the univalent nature of Mg^{2+} is more effective at generating oxygen vacancies in the alumina lattice than the variable-valent cobalt ions, and the Ni-Al composite structure is the most effective of all.

Collectively, the superior stability and regenerability of the 10Ni/NiAl catalyst stem from a synergistic effect: 1) a strong electronic interaction (evidenced by Ni 2p XPS) that anchors the active Ni phase, and 2) the creation of a uniquely high concentration of surface oxygen vacancies (quantified by O 1 s XPS) that enhances the catalyst's redox flexibility.

3.3. Characterization of the spent Ni-based catalysts

Fig. 4 presents the XRD and H_2-TPR results after the MSR process at the WHSV of 240,000 mL/(h·g_{cat}). As shown in Fig. 4(a), all catalysts exhibit distinct diffraction peaks corresponding to NiO at 2θ values of 43.3°, 62.9° and 75.4°, indicating that a portion of the metallic Ni has been oxidized to NiO during the reaction. Notably, the NiO peaks for the 10Ni/NiAl catalyst are relatively weaker, suggesting a lower extent of Ni oxidation. Moreover, only the 10Ni/NiAl catalyst retains pronounced diffraction peaks of metallic Ni at 44.5°, 51.8°, and 76.4°, whereas these characteristic peaks are absent in the other samples. This observation indicates that a significant amount of Ni^0 remains in the 10Ni/NiAl catalyst after the reaction, which is likely one of the reasons for its superior catalytic activity.

Comparing Fig. 4(b) with Fig. 3(c) reveals a notable reduction in the peak area of the low and medium temperature reduction peaks for all catalysts, except for the 10Ni/NiAl sample. Simultaneously, the spinel reduction peaks at approximately 1100 K are significantly larger for the 10Ni/MgAl, 10Ni/CoAl, 10Ni/Al, and 20Ni/Al catalysts. This suggests that the most of the nickel species on the surface of these catalysts have been converted to $NiAl_2O_4$, which likely leads to a decrease in catalytic activity [29].

The reduction peak profile of the 10Ni/NiAl catalyst exhibits remarkable stability before and after the reaction, with only minimal fluctuations observed. This stability stands in stark contrast to the pronounced changes in reduction behavior seen in other catalysts, indicating that a substantial amount of NiO remains readily reducible on the surface of 10Ni/NiAl. During the reaction, the emergence of a reduction peak at 530 K confirms the formation of more easily reducible nickel species. This suggests that part of the oxidized nickel undergoes further activation, forming a "free-state" NiO configuration that participates in a dynamic redox cycle between Ni^0 and Ni^{2+}. Such activated species are associated with enhanced reactivity, thereby contributing to improved catalytic performance.

Meanwhile, the overall shift of the reduction peaks toward higher temperatures, along with the emergence of a high-temperature peak at approximately 1053 K, indicates that a minor fraction of nickel oxide interacts with alumina to form the $NiAl_2O_4$ phase. However, the extent

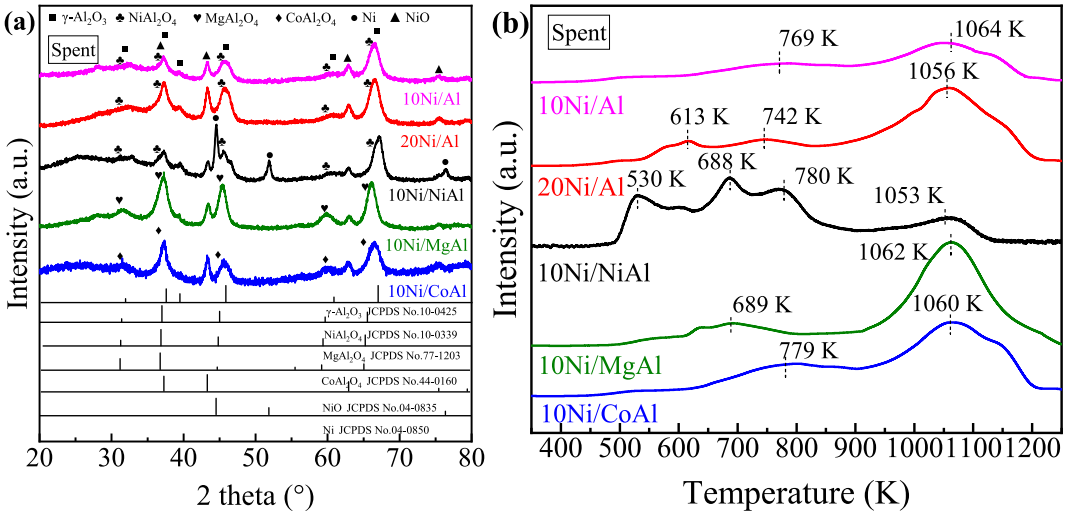

Fig. 4. Characterization of the catalysts after 20 h of MSR at WHSV = 240,000 mL/(h·g_{cat}). (a) XRD patterns. (b) H_2-TPR profiles.

of this interaction appears to be limited, as evidenced by only a slight increase in the corresponding peak area.

The collective results, encompassing the stability of reduction peaks, the limited formation of $NiAl_2O_4$, the preservation of catalytically active nickel oxide species, and the activation of a substantial portion of nickel oxide, collectively elucidate the remarkable catalytic activity demonstrated by the 10Ni/NiAl catalyst. This exceptional performance underscores the significant potential of this catalyst for a diverse array of applications that require both high activity and stability.

3.4. Forced coke deposition by methane decomposition

Fig. 5 illustrates the catalytic performance of different catalysts after methane decomposition. As evident from the figure, with the notable exception of the 10Ni/CoAl catalyst, the catalytic activities of the other samples have predominantly reverted to its initial levels. During the methane decomposition, a minor amount of H_2 was detected. This can be attributed to the catalytic decomposition of methane by Ni and Co, both of which are transition metals known for their ability to catalyze this reaction at 973 K, as reported in previous studies [51–54].

Therefore, a small amount of H_2 is generated during the process of methane decomposition [55,56]. Methane and hydrogen, both considered as clean and renewable energy sources, are widely used as reductants to reduce metal oxides. Reza Alizadeh has reported that the successful reduction of nickel oxide to metallic nickel by methane within the temperature range of 873–998 K [57]. Melek Cumbul Altay has confirmed the complete reduction of nickel oxide with low Ni content in the H_2 atmosphere at 625 K, which coincides with the temperature at which methane initiates the reduction of nickel oxide [58].

Following two instances of methane exposure, the activity of the 10Ni/CoAl sample has decreased to a certain extent, with the methane conversion rate diminishing to approximately 80 %, accompanied by a corresponding decrease in hydrogen yield.

When methane purged occurs, the main reaction is methane decomposition reaction (1), which is an important method for producing carbon nanotubes and carbon nanofibers [59–61]. These residual species could it is important to note that trace amounts of water, carbon monoxide, and carbon dioxide may remain in the system from the previous steam reforming reaction, such as reactions (2), (3), and (4), thereby influencing the overall catalytic performance.

$$CH_4 \rightarrow C + 2H_2, \Delta H_{298K} = +74.52\ \text{kJ/mol} \quad (1)$$

$$CO_2 + 3H_2 \rightarrow CH_4 + H_2O, \Delta H_{298K} = -165\ \text{kJ/mol} \quad (2)$$

$$CH_4 + H_2O \rightarrow CO + 3H_2, \Delta H_{298K} = +206\ \text{kJ/mol} \quad (3)$$

$$CO + H_2O \rightarrow CO_2 + H_2, \Delta H_{298K} = -41.2\ \text{kJ/mol} \quad (4)$$

Moreover, high-performance catalysts such as the 10Ni/NiAl catalyst exhibit remarkable methane conversion rates, achieving up to 98 % at 973 K. Under these conditions, the outlet gas composition comprises over 80 % hydrogen, accompanied by an excess of steam. This environment poses significant challenges for the deposition of carbon from methane on the catalyst surface, as the abundant water vapor inhibits stable carbon deposit formation.

Francois-Xavier Chiron has discovered that methane interacts with active nickel sites on the $NiO/NiAl_2O_4$ catalyst, resulting in the formation of coke deposits [62]. However, these deposits can be effectively alleviated through steam-carbon gassing reactions, which consume the coke and produce a concentrated stream of CO/H_2. Therefore, even in instances where carbon deposition occurs, its effect can be substantially reduced by the presence of excess steam.

As mentioned previously, carbon deposition may contribute to the deactivation of the 10Ni/CoAl catalyst, although it is not the sole factor responsible for catalyst deactivation. The restoration of catalyst activity following methane purged can be attributed to the efficient reduction of nickel oxide in both methane and hydrogen environments.

After the methane treatment test, carbon was deposited on the catalyst surface in the form of coke, a byproduct of methane cracking. To evaluate the carbon accumulation performance of different catalysts, TGA was performed, and the results are presented in Fig. 6(a). The weight losses measured for the10Ni/Al, 20Ni/Al, 10Ni/NiAl, 10Ni/MgAl, and 10Ni/CoAl catalysts were 29.1 %, 25.1 %, 17.7 %, 23.0 %, and 19.0 %, respectively. Among these, the 10Ni/NiAl catalyst exhibited the lowest carbon deposition, indicating its strong resistance to this deactivation pathway.

The spent 10Ni/NiAl catalyst shows a high D-to-G band intensity ratio (I_D/I_G) of 1.39, characteristic of disordered, amorphous carbon. In contrast, the 10Ni/Al catalyst displays a much lower I_D/I_G ratio of 1.23, indicating the formation of more ordered, graphitic carbon (Fig. 6(b)) [2,32,56]. These findings corroborate the TGA results, linking lower carbon amounts to less graphitic structures.

The lower carbon deposition on the 10Ni/NiAl catalyst can be attributed to the combined effects of its well-dispersed Ni particle size distribution, enhanced surface basicity, and strong MSI, which together inhibit graphitic carbon formation and promote the gasification of carbon precursors.

To understand the mechanism behind this resistance, the nature and morphology of the deposited carbon were investigated by TEM, which

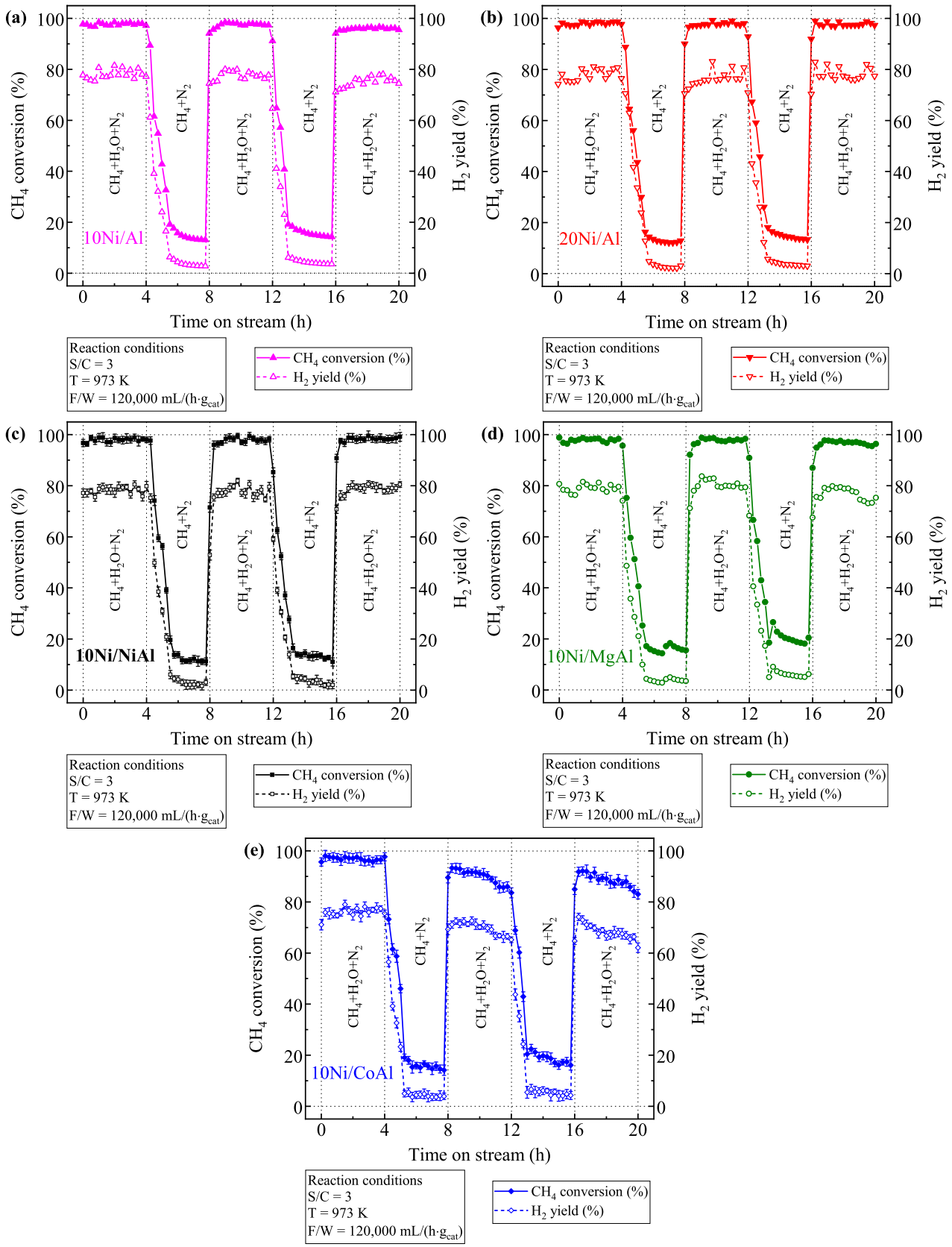

Fig. 5. Catalytic performance during the forced coke deposition test, cycling between MSR and dry methane streams. (a) 10Ni/Al, (b) 20Ni/Al, (c) 10Ni/NiAl, (d) 10Ni/MgAl, (e) 10Ni/CoAl.

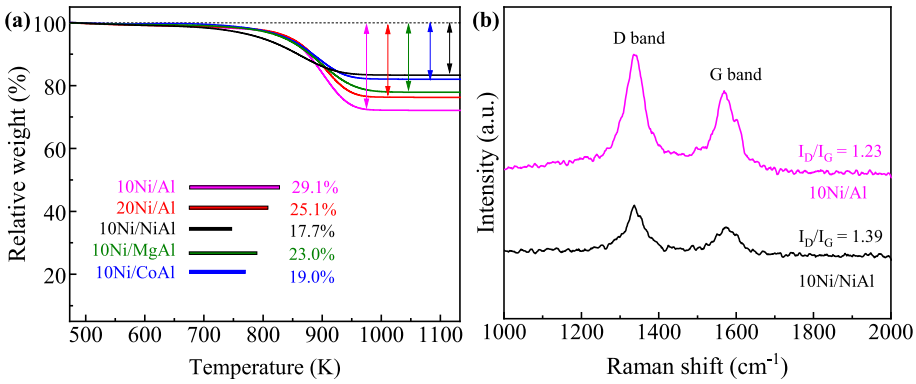

Fig. 6. TGA profiles (a) and Raman spectra (b) of spent catalysts after the forced coke deposition test.

provide a striking visualization of the underlying cause. The spent 10Ni/Al catalyst (Fig. S6(a)) revealed severe Ni sintering, with large particles promoting filamentous carbon nanotube growth [29]. Conversely, the 10Ni/NiAl catalyst (Fig. S6(b)) maintained small, well-dispersed Ni nanoparticles without agglomeration, thereby inhibiting filamentous coke formation.

Collectively, these analyses indicate that strong MSI in the 10Ni/NiAl catalyst mitigate Ni sintering–a key precursor to filamentous coke nucleation. This results in reduced carbon deposition and a preference for amorphous over graphitic forms, accounting for its superior performance in resisting deactivation.

3.5. High-temperature force sintering experiment

Fig. 7 illustrates the effect of forced sintering treatment at 1223 K on the activity of various catalysts. As indicated, only the 10Ni/CoAl catalyst experienced a decline in activity following 12 h of forced sintering, whereas the remaining catalysts have exhibited high level of resistance to sintering. Prior to the forced sintering treatment, the catalytic activity of 10Ni/CoAl remained relatively stable, but a gradual decrease was observed during prolonged high-temperature exposure. This suggests that the performance deterioration of the 10Ni/CoAl catalyst is primarily attributable to the sintering of nickel crystallites, whereas sintering does not appear to be a significant deactivation pathway for the other catalysts. Moreover, although forced sintering did not compromise the high-temperature catalytic activity, it adversely affected the low-temperature performance. Additionally, the longer the sintering duration, the more pronounced the loss of activity, as shown in Fig. S7.

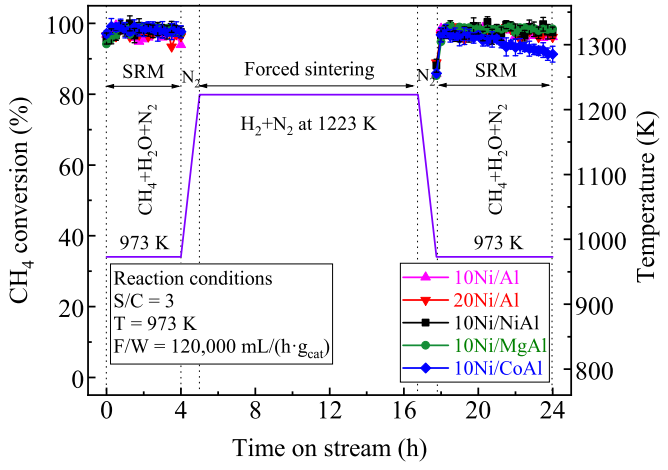

Fig. 7. Catalytic activity before and after a forced sintering treatment (1223 K, H_2/N_2, 12 h).

Fig. 8 shows that the 10Ni/NiAl catalyst is the only one that exhibited XRD diffraction peaks of reduced Ni (at approximately 44.5°, 51.9°, and 76.4°) after high-temperature sintering. These peaks were not observed in the other four catalysts. Furthermore, there are prominent NiO characteristic peaks at approximately 43.3°, 62.9° and 75.4°. However, the NiO peaks in the 10Ni/NiAl catalyst were broader and shorter in duration compared to those in the other catalysts, suggesting that nickel is primarily present in its reduced state in the spent 10Ni/NiAl catalyst. It also suggests that the other catalysts are more likely to form $NiAl_2O_4$.

3.6. Steam induced oxidation

Following steam treatment at 923 K, a significant decline in catalytic activity was observed for most catalysts, with conversion dropping below 10 %. In contrast, the 10Ni/NiAl catalyst demonstrated remarkable thermal and structural resilience, as its catalytic performance was fully restored upon reactivation in the steam reforming reaction at 973 K, reaching levels comparable to those prior to steam exposure (Fig. 9).

This finding underscores the unique properties of the 10Ni/NiAl

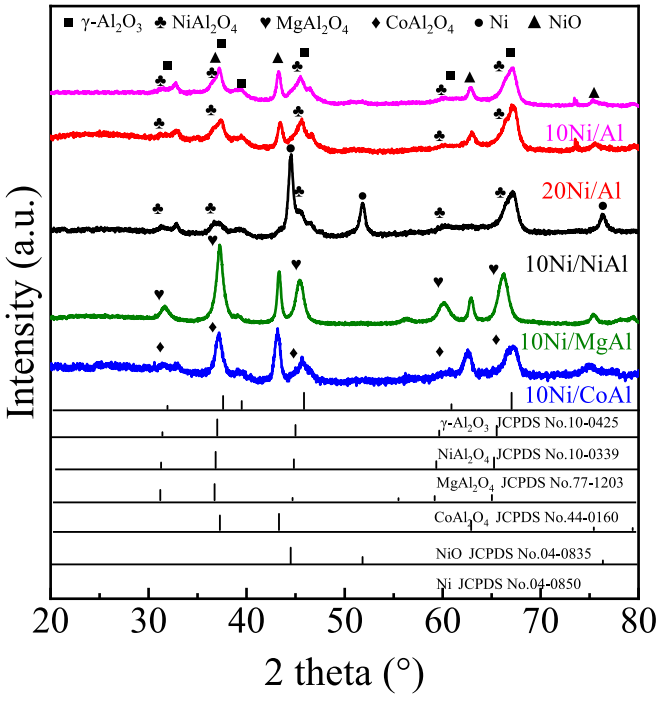

Fig. 8. XRD patterns of the catalysts after the forced sintering treatment at 1223 K.

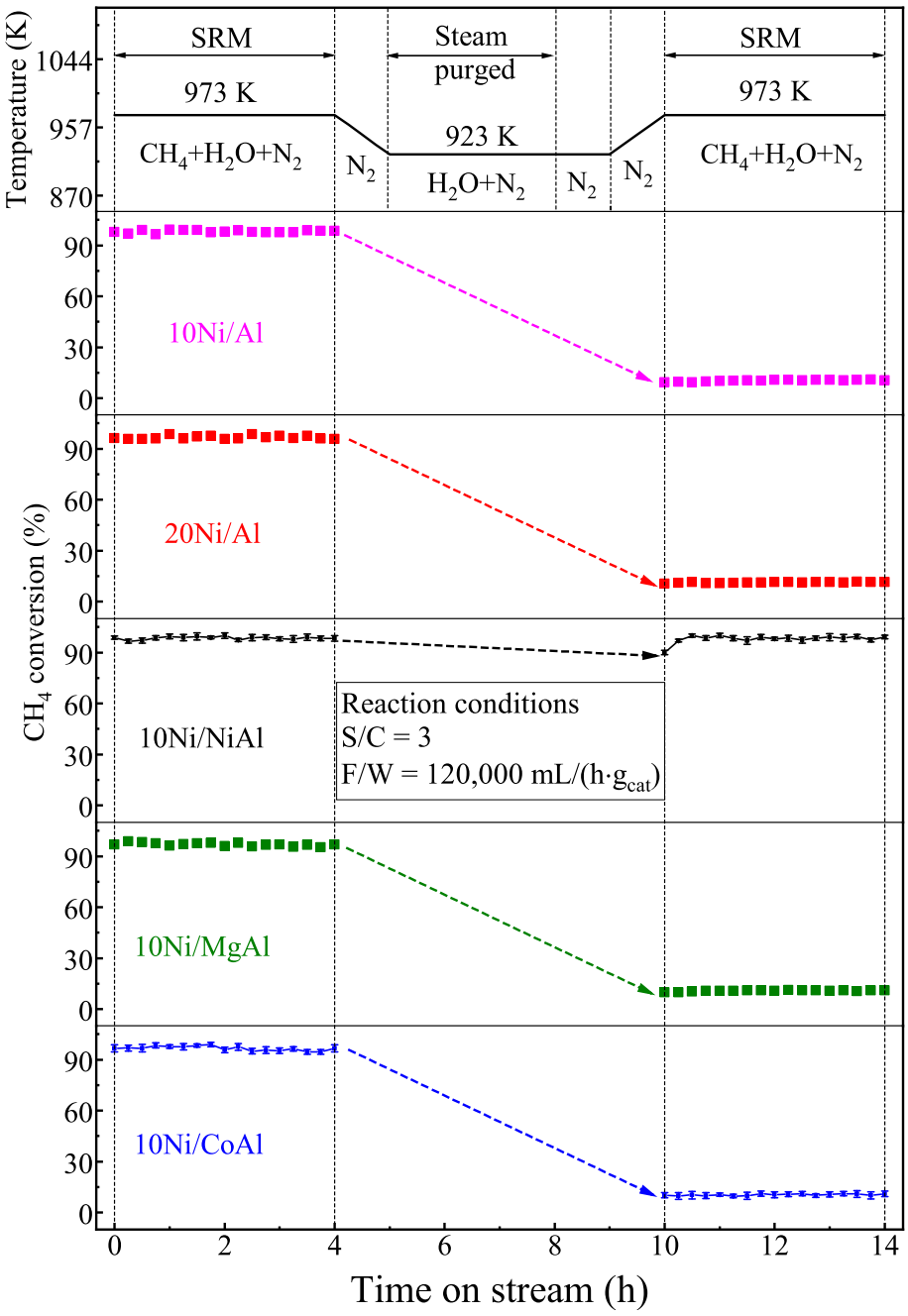

Fig. 9. Catalytic activity showing the effect of steam treatment (923 K, H_2O/N_2) on different catalysts.

catalyst, which enable it to withstand the adverse effects of steam treatment and effectively recover its activity. It suggests that the catalyst may possess enhanced structural stability and the ability to preserve its active sites during steam purged. Alternatively, the catalyst may exhibit efficient mechanisms for regenerating its active sites after steam treatment.

Comparison with Fig. 2(b) and (c), the distinctive peaks of Ni and NiO disappeared for all catalysts except 10Ni/NiAl (Fig. 10(a)). Instead, the diffraction peaks at approximately 37.0°, 45.0°, and 67.0° increased in intensity, corresponding to of γ-Al_2O_3 and $NiAl_2O_4$. This increase indicates the progressive growth and crystallinity enhancement of $NiAl_2O_4$, while alumina content remains unchanged. For the 10Ni/NiAl catalyst, the XRD pattern after steam treatment at 923 K remained similar to that in Fig. 4(a), with well-preserved metallic Ni diffraction peaks, confirming its superior resistance to steam oxidation due to the pre-formed $NiAl_2O_4$-like support structure that stabilizes Ni and suppresses further transformation into catalytically inert spinel.

This "Ni-to-spinel" transformation is precisely the core mechanism of irreversible deactivation under steam. Under high-temperature steam conditions, active metallic Ni^0 sites are readily oxidized to NiO. Due to the close contact between this newly formed NiO and the alumina support, a solid-state reaction occurs to generate thermodynamically stable $NiAl_2O_4$. As shown in the H_2-TPR results (Fig. 10(b)), the reduction temperature of $NiAl_2O_4$ exceeds 993 K, much higher than the MSR reaction temperature (973 K) and typical regeneration temperatures. Consequently, once Ni species are incorporated into the spinel lattice, they cannot be reduced back to their active metallic state under operational conditions, leading to a permanent reduction in active sites and ultimately irreversible deactivation.

As demonstrated in the previous methane decomposition-induced

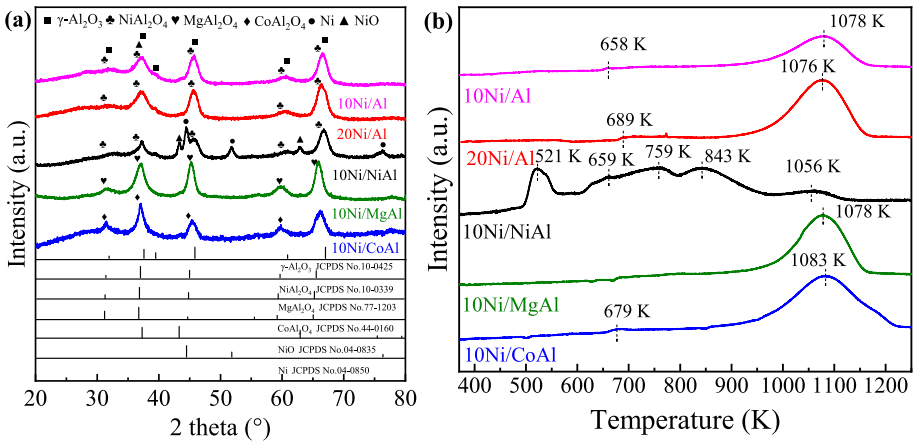

Fig. 10. Characterization of catalysts after steam treatment at 923 K. (a) XRD patterns. (b) H_2-TPR profiles.

coking experiments, both methane and the hydrogen from its cracking can act as reducing agents. Therefore, after eliminating steam exposure, nickel oxide can be reduced, causing activity to quickly return to its initial state.

Fig. 10(b) displays the H_2-TPR profiles of various catalysts after steam treatment at 923 K. Compared with the fresh samples (Fig. 3), the low- and medium-temperature NiO reduction peaks almost disappear for all catalysts except 10Ni/NiAl, while the high-temperature peak (~993 K) becomes significantly more intense. This suggests that the majority of Ni species are converted into a spinel-type structure after steam exposure, which is consistent with the XRD results shown in Fig. 10(a).

In contrast to the spent catalysts after 20 h of methane steam reforming (Fig. 4(b)), the structural transformation induced by the 923 K steam treatment is more pronounced. The samples in Fig. 4(b) still retain part of the low-temperature reduction peak, whereas a complete disappearance of these peaks is observed after only 3 h of steam treatment (Fig. 10(b)). Simultaneously, the high-temperature peaks not only dominate the profiles but also shift to higher temperatures, indicating that the steam treatment more effectively promotes the incorporation of Ni into the spinel phase, leading to stronger metal–support interactions and a higher degree of structural stabilization.

For the 10Ni/NiAl catalyst, steam treatment results in a weakened medium-temperature peak and an overall shift of the reduction profile toward higher temperatures, compared with its fresh counterpart (Fig. 3(c)). Relative to the sample after 20 h of reaction (Fig. 4(b)), the proportion of low-temperature peaks decreases while the high-temperature peak slightly intensifies. Notably, a new reduction peak appears at 521 K after steam treatment, closely resembling the 530 K peak observed after long-term reaction. This may indicate the generation of highly redox-active Ni species during the treatment, which may be key to maintaining its activity.

The combined XRD and TPR analyses indicate that Mg and Co-doped composite oxide supports exhibit reduced resistance to steam oxidation than Ni-doped supports. Specifically, the readily reducible NiO in the 10Ni/NiAl catalyst acts as a reversible redox reservoir ($Ni^0 \leftrightarrow NiO$), maintaining activity during steam exposure and subsequent reforming. In contrast, in MgAl- and CoAl-supported catalysts, Ni species are more readily incorporated into stable spinel phases ($MgAl_2O_4$, $CoAl_2O_4$), which require much higher reduction temperatures and therefore lead to irreversible deactivation. This finding suggests that the 10Ni/NiAl catalyst possesses robust resistance to hydrothermal degradation.

To systematically investigate the effect of steam treatment temperature on the structural and catalytic properties of the catalyst, 10Ni/NiAl was selected as a representative sample. In addition to the treatment at 923 K, two higher-temperature treatments at 948 and 973 K were introduced. The samples were subsequently characterized by XRD and H_2-TPR, as shown in Fig. 11.

As depicted in Fig. 11(a), when the steam treatment temperature increased from 923 K to 948 K, the characteristic diffraction peaks of metallic Ni^0 at 44.5°, 51.8°, and 76.4° gradually disappeared, accompanied by a significant increase in the peak intensities at 45.0° and 67.0°. According to the Fig. 2(a), these changes can be ascribed to the enhanced formation of the $NiAl_2O_4$ spinel phase. Further raising the temperature to 973 K led to a substantial decrease in the intensity of NiO-related peaks at 43.3°, 62.9°, and 75.4°, with a concomitant further enhancement of the $NiAl_2O_4$ peaks. These results indicate a progressive transformation of Ni species into the thermodynamically stable $NiAl_2O_4$ phase under high-temperature steam treatment. Compared with other catalysts treated at 923 K (Fig. 10(b)), where NiO reflections nearly vanished, the persistence of NiO peaks in 10Ni/NiAl suggests superior resistance to structural degradation under hydrothermal conditions.

Fig. 11(b) shows the H_2-TPR profiles of the steam-treated samples. All samples exhibited considerable reducibility, yet the reduction peaks systematically shifted toward higher temperatures with increasing treatment temperature. At 948 K, the high-temperature reduction peak became dominant while the intensities of the low- and medium-temperature peaks were significantly suppressed, indicating partial transformation of NiO into $NiAl_2O_4$ with stronger MSI. When the treatment temperature reached 973 K, only a broad high-temperature peak remained, with an onset temperature as high as 1086 K, reflecting the presence of strongly bound $NiAl_2O_4$ species. This reduction behavior resembles that of other catalysts treated at 923 K (Fig. 10(b)), confirming the formation of a spinel structure with enhanced thermal stability and poor reducibility. These results are in good agreement with the XRD analysis.

The influence of steam treatment temperature on catalytic activity is further illustrated in Fig. 11(c). A notable decline in CH_4 conversion was observed even when the treatment temperature was raised by only 298 K, suggesting a rapid deactivation process. At 948 K, the catalyst exhibited a marked loss of activity, which became even more severe at 973 K. Combined with the XRD and H_2-TPR data, this deactivation is primarily attributed to the irreversible transformation of active Ni^0 and NiO species into catalytically inert $NiAl_2O_4$, resulting in a significant reduction in the number of accessible active sites.

In summary, high-temperature steam treatment promotes the formation of the $NiAl_2O_4$ spinel phase, which, despite its structural stability, exhibits poor catalytic activity. This transformation is the primary cause of performance degradation. Notably, the 10Ni/NiAl catalyst treated at 923 K retained a considerable level of activity, demonstrating superior hydrothermal stability and structural resistance compared to other samples.

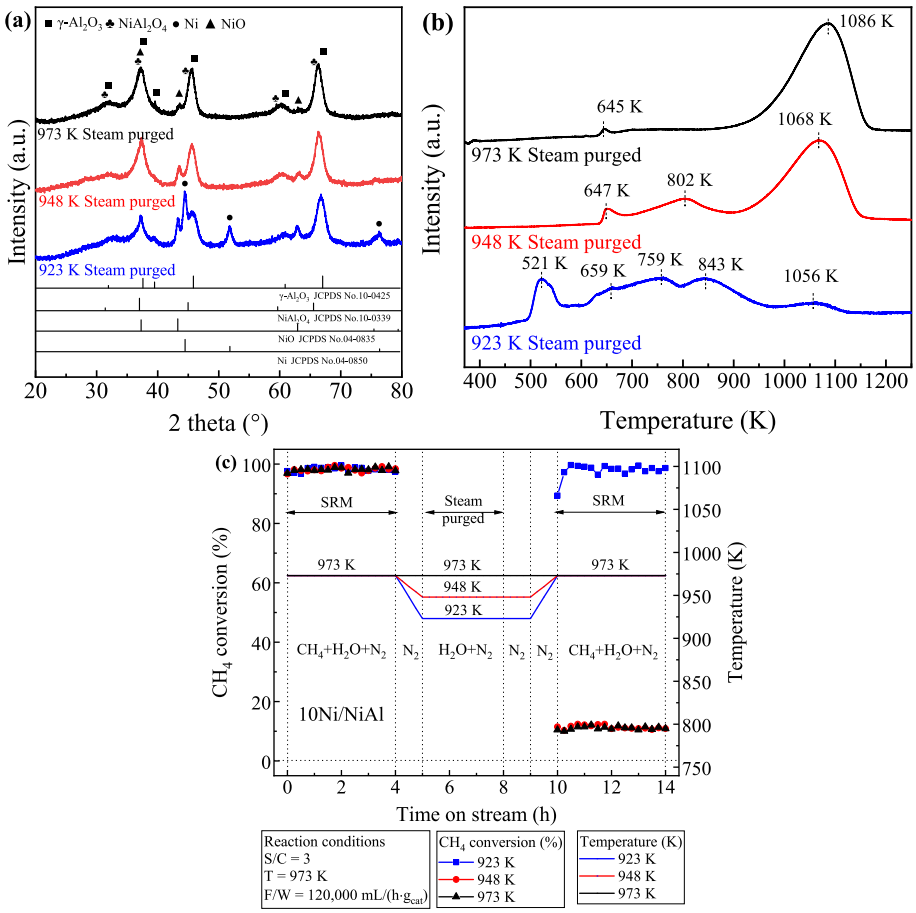

Fig. 11. Effect of steam treatment temperature on the 10Ni/NiAl catalyst. (a) XRD patterns. (b) H_2-TPR profiles. (c) Catalytic activity tests after treatment at 923 K, 948 K, and 973 K.

3.7. Effect of H_2 and steam on the oxidation resistance of 10Ni/Al catalyst

Fig. 12 illustrates the time-on-stream performance of the 10Ni/Al catalyst under varying inlet hydrogen flow rates and steam-to-carbon (S/C) ratios at 973 K and a space velocity of 240,000 mL/(h·g_{cat}). As observed in Fig. 1(b), all catalysts except 10Ni/NiAl exhibited pronounced deactivation under the tested conditions. Therefore, the 10Ni/Al catalyst, which displayed relatively poor stability, was selected for further investigation to assess the effects of H_2 co-feeding and steam content on catalytic durability.

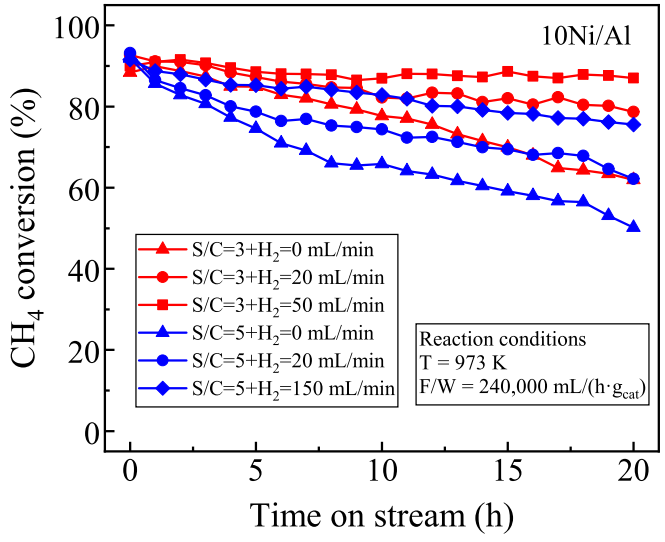

Fig. 12. Effect of co-feeding H_2 at different steam-to-carbon (S/C) ratios on the stability of the 10Ni/Al catalyst.

The red curves correspond to an S/C ratio of 3, while the blue curves represent S/C = 5. Under S/C = 3 conditions, increasing the inlet H_2 flow from 0 to 50 mL/min (from red triangle to red square markers) exhibits a marked improvement in catalyst stability. Notably, when 50 mL/min of H_2 is introduced, the CH_4 conversion remains relatively stable over 20 h, indicating effective suppression of catalyst deactivation. This stabilization effect is primarily attributed to the role of H_2 in preserving the metallic Ni^0 phase, thereby preventing oxidation-induced deactivation.

In contrast, under S/C = 5 conditions (blue curves), even increasing the H_2 flow from 0 to 150 mL/min still fails to maintain stable activity, as CH_4 conversion continuously declines regardless of the H_2 content. Specifically, at the highest H_2 flow rate tested, only limited improvement in catalytic stability is observed. This suggests that the excessive steam at high S/C ratios dominates the surface redox environment, facilitating the oxidation of active Ni sites. The primary cause of deactivation in this case is the steam-induced oxidation of the Ni surface, which overrides the protective effect of co-fed H_2.

Overall, while H_2 co-feeding is effective in enhancing the stability of Ni-based catalysts under moderate steam conditions, its protective effect is substantially diminished at elevated S/C ratios due to steam-induced oxidation. This emphasizes the need for an optimal integration of both H_2 addition and steam content to ensure long-term catalyst durability under conditions relevant to reforming-based hydrogen production.

3.8. Comprehensive evaluation with 10Ni/NiAl

The 10Ni/NiAl catalyst was systematically evaluated under three accelerated deactivation protocols simulating extreme industrial operating conditions: (1) transient hydrothermal aging (923 and 973 K), (2) forced carbon deposition via methane decomposition, (3) high-temperature thermal aging at 1223 K to induce sintering. As depicted in Fig. 13, the catalyst exhibited distinct responses to these sequential challenges. After steam treatment at 923 K, the catalyst fully recovered its activity (<1 % conversion loss) through in situ reduction, consistent with previous findings (Fig. 10). In contrast, steam purged at 973 K led to irreversible deactivation, with approximately 90 % loss in methane conversion, in agreement with the results shown in Fig. 11(c). H_2-TPR results (Fig. 11(b)) confirmed that high-temperature hydrogen treatment (> 1086 K) effectively reduced the spinel phase, enabling recovery of the initial activity comparable to that of the fresh catalyst. After regeneration, the catalyst demonstrated excellent stability during subsequent forced deactivation tests, maintaining 98±0.5 % methane conversion under methane purged conditions and following thermal sintering. This dual resistance to both carbon deposition and thermal degradation is attributed to strong metal-support interactions, which inhibit nickel migration while preserving active sites. Notably, the sequential deactivation–regeneration cycles resulted in minimal irreversible activity loss, significantly outperforming conventional Ni/Al_2O_3 catalysts.

The regeneration mechanism is primarily governed by the thermally activated reduction of $NiAl_2O_4$, which becomes irreducible below 1056 K, as evidenced in H_2-TPR profiles (Fig. 11(b)). This temperature-dependent reducibility explains the permanent deactivation observed at 973 K and the subsequent activity recovery at 1123 K. This regenerative capability, combined with inherent structural stability, highlights the promise of 10Ni/NiAl as a thermally resilient catalyst for MSR systems operating under frequent thermal cycling.

In summary, these findings provide new insights into hydrothermal deactivation mechanisms in Ni-based catalysts and establish quantitative performance benchmarks under harsh operating conditions. The demonstrated regeneration capability through controlled hydrogen treatment offers practical strategies to extend catalyst lifetimes in industrial hydrogen production, particularly in systems powered by intermittent renewable energy sources.

3.9. Long-term stability evaluation of 10Ni/NiAl

The spherical 10Ni/NiAl catalyst (Fig. S8) with optimized morphology was synthesized to improve its suitability for large-scale hydrogen production applications. To evaluate the operational robustness of the catalysts in the absence of inert gas, long-term stability tests were conducted using a reforming reaction system (Fig. S9) integrated with a 5 kW high-power fuel cell diagnostic system (Fig. S10). The catalytic performance was assessed in a tubular reactor (Fig. S11) under thermochemical conditions designed to simulate real-world operation (T = 973 K, P = 1 bar).

The time-on-stream analysis revealed exceptional catalytic durability, with less than 5 % activity loss observed over the first 300 h of continuous operation (Fig. 14). Notably, the catalyst exhibited full recovery of its initial conversion efficiency (98.5±0.5 %) upon system restart, maintaining stable performance (CH_4 conversion: 97.8±0.6 %) during five subsequent 50 h operational cycles.

This reversible behavior under multiple dynamic DSS conditions suggests remarkable structural stability and resistance to common deactivation mechanisms, such as coking or metal sintering. These findings confirm the catalyst can withstand repeated thermal cycling and prolonged exposure to reforming reaction environments without significant deactivation. The demonstrated combination of multiple restart capabilities and long-term stability positions this 10Ni/NiAl catalyst as a promising candidate for commercial hydrogen production systems, particularly those requiring intermittent operation or load-following capabilities.

3.10. Comparison with literature

To comprehensively evaluate the performance of the 10Ni/NiAl catalyst developed in this study, a comparison with recently reported state-of-the-art Ni-based catalysts for MSR is presented (Table S2).

As shown in Table S2, previous works have enhanced Ni-based catalyst activity and stability using strategies such as noble metal doping, bimetallic alloying, core-shell structures, or novel supports. A critical challenge in MSR catalysis, especially for decentralized fuel cell-integrated applications, is maintaining stability under high space velocities and dynamic conditions. While many reported catalysts exhibit good initial activity, they are often tested at WHSV values below 100,000 mL/(h·g_{cat}). In contrast, the 10Ni/NiAl catalyst demonstrates stable performance (CH_4 conversion > 95 %) at a high WHSV of 240,000 mL/(h·g_{cat}), where conventional catalysts deactivate rapidly.

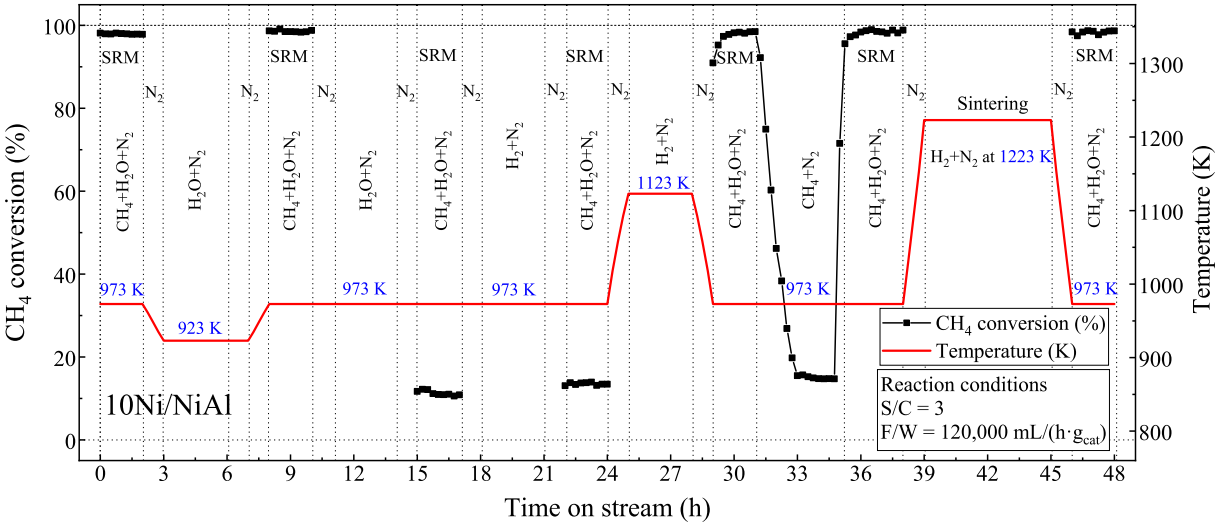

Fig. 13. Comprehensive performance of the 10Ni/NiAl catalyst under sequential deactivation protocols simulating steam treatment, methane decomposition, and high-temperature sintering.

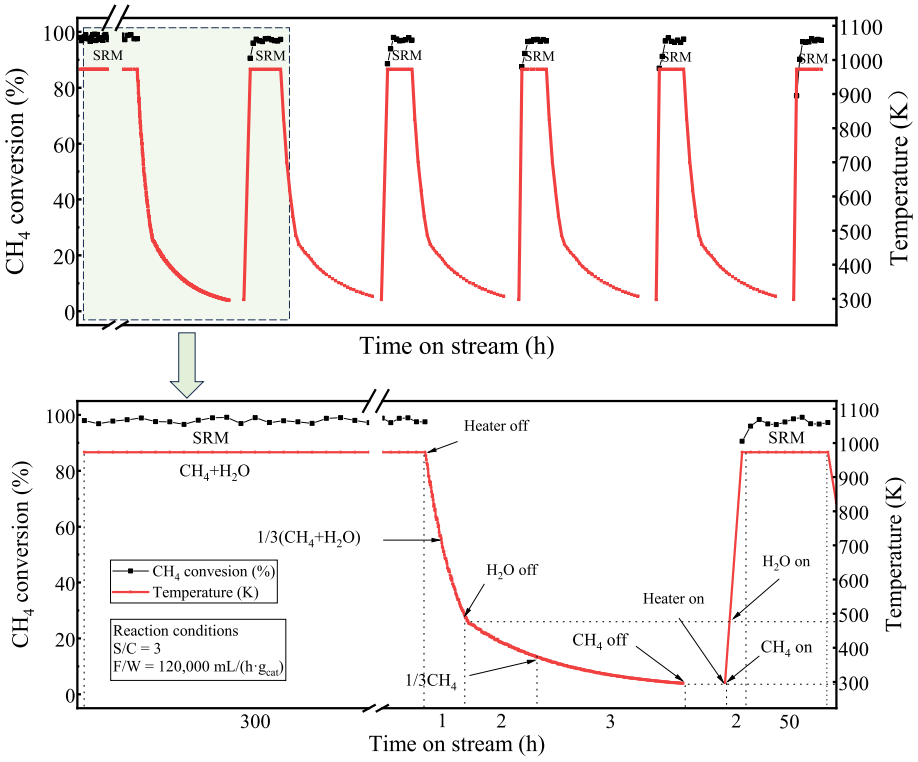

Fig. 14. Long-term stability test of the 10Ni/NiAl catalyst, including multiple start-up/shut-down (DSS) cycles, integrated with a 5 kW fuel cell system.

The key advantage lies in its structural resilience and regenerability after exposure to severe deactivation protocols (high-temperature steaming, forced coking, and sintering), including full activity recovery post-steam deactivation–a feature seldom reported. This durability suits applications requiring frequent cycles and long-term robustness.

4. Conclusions

Composite metal oxide supports (NiO-Al_2O_3, MgO-Al_2O_3, and Co_3O_4-Al_2O_3) were synthesized and impregnated with Ni to prepare Ni-based catalysts. The influence of the supports on catalyst stability was systematically evaluated. This study comprehensively explored the deactivation mechanisms of Ni-based catalysts during MSR under high-temperature hydrothermal conditions. Key causes of catalyst deactivation–carbon deposition, oxidation by steam, and sintering-were identified through a series of accelerated deactivation tests, including methane, steam, and hydrogen treatments.

Among the tested catalysts, the 10Ni/NiAl catalyst exhibited superior catalytic performance and stability, particularly under high WHSV conditions of 240,000 mL/(h·g_{cat}). It demonstrated remarkable resilience to steam exposure at 923 K, whereas the other catalysts experienced complete loss of activity. Post-treatment characterization revealed that 10Ni/NiAl catalyst retained partially reduced Ni species and easily reducible NiO, which could be reactivated by H_2 or CH_4, enabling rapid recovery of catalytic activity. In contrast, the other catalysts underwent irreversible deactivation due to the complete oxidation of Ni to the inert $NiAl_2O_4$ phase.

Methane decomposition at 973 K caused minimal deactivation, with the 10Ni/NiAl catalyst showing the lowest carbon deposition (17.02 %). Under severe hydrogen treatment at 1223 K, only the 10Ni/CoAl catalyst exhibited a slight decline in activity. The enhanced stability of the catalysts was attributed to the formation of NiAl composite metal oxides during high-temperature calcination, which effectively anchored the Ni nanoparticles, preventing sintering and inhibiting the formation of the less reducible $NiAl_2O_4$ phase.

The 10Ni/NiAl catalyst displayed exceptional operational stability, maintaining consistent performance for over 300 h in a 5 kW fuel cell reforming application and achieving full recovery after start-up and shut-down cycles. Synthesized via industrially viable co-precipitation and impregnation methods, it offers costs comparable to commercial catalysts due to similar elemental compositions, while its simpler makeup enables easier recycling and lower environmental impact than complex formulations, promoting sustainability for industrial-scale use.

These results highlight 10Ni/NiAl catalyst's superior regenerability and coking resistance under harsh hydrothermal and high–WHSV conditions, positioning it as a promising candidate for decentralized MSR–SOFC systems with fluctuating operations.

CRediT authorship contribution statement

Yi Lin: Writing – original draft, Validation, Software, Investigation, Formal analysis, Data curation, Conceptualization. **Zaixing Wang:** Visualization, Software, Data curation. **Lina Tang:** Validation, Supervision, Resources. **Shi Jiang:** Supervision, Project administration, Methodology, Funding acquisition. **Yu Guo:** Writing – review & editing, Supervision, Software, Resources, Project administration, Funding acquisition, Formal analysis, Conceptualization. **Xiaoqin Liu:** Writing – review & editing, Visualization, Methodology, Conceptualization.

Declaration of competing interest

The authors declare that they have no known competing financial interests or personal relationships that could have appeared to influence the work reported in this paper.

Acknowledgments

The support of this work by the Science and Technology Project of Zhejiang Zheneng Technology & Environment Group Co., Ltd. (No. TD-KJ-23-005), the National Natural Science Foundation of China (No. 22108116) and the Independent Research Project of the State key Laboratory of Materials-oriented Chemical Engineering (No. SKL-MCE-

24A13) is gratefully acknowledged.

Appendix A. Supplementary data

Supplementary data to this article can be found online at https://doi.org/10.1016/j.fuproc.2025.108325.

Data availability

Data will be made available on request.

References

[1] J. Zhang, M. Zhao, Z.W. Yin, Z.Y. Hu, Y. Liu, Y. He, D. Li, Modification of Al_2O_3-based catalyst by rare earth elements for steam reforming of methane, AICHE J. 69 (2023) e18070.

[2] W. Zeng, L. Li, M. Song, X. Wu, G. Li, C. Hu, The effect of different atmosphere treatments on the performance of Ni/Nb-Al_2O_3 catalysts for methane steam reforming, Int. J. Hydrog. Energy 48 (2023) 6358–6369.

[3] N. Zhang, B. Wang, P. Hu, Z. Gao, H. Wang, Achieve high-efficiency photocatalytic hydrogen production of MCNTs-CdS/Pt/$ZnFe_2O_4$ heterojunction owing to building charge transport bridge, J. Environ. Chem. Eng. 13 (2025) 115800.

[4] Y. Ma, B. Wang, H. Wang, X. Zhao, Y. Zhao, S. Wu, C. Xie, Microstructure regulation and photocatalytic H_2 evolution mechanism of novel MCNTs-$Zn_{0.3}Cd_{0.7}S$/Pd composites, Int. J. Hydrog. Energy 126 (2025) 484–495.

[5] J. Zhang, Z. Xiao, L. Wang, X. Zhang, G. Li, Balancing Ni^0 and Ni^{2+} on γ-Al_2O_3 for efficient steam methane reforming, ChemistrySelect 7 (2022) e202203339.

[6] H. Ito, Economic and environmental assessment of residential micro combined heat and power system application in Japan, Int. J. Hydrog. Energy 41 (2016) 15111–15123.

[7] Z. Wang, J. Mao, Z. He, F. Liang, Energy-exergy analysis of an integrated small-scale LT-PEMFC based on steam methane reforming process, Energy Convers. Manag. 246 (2021) 114685.

[8] Z. Wang, Y. Lin, J. Mao, F. Liang, Z. He, Y. Guo, J. Hu, R. Xu, Performance analysis of a multi-fuel reforming variable-power generation system: a forward-backward thermodynamic approach, Energy Convers. Manag. 315 (2024) 118765.

[9] Y. Guo, X. Guo, H. Zhang, S. Hou, Energetic, exergetic and ecological analyses of a high-temperature proton exchange membrane fuel cell based on a phosphoric-acid-doped polybenzimidazole membrane, Sustain Energy Technol Assess 38 (2020) 100671.

[10] E. Baniasadi, F. Ghojavand, C.O. Colpan, Y. Devrim, Performance analysis of a gas-to-power system based on protonic-ceramic electrochemical compressor, Int. J. Hydrog. Energy 48 (2023) 36836–36848.

[11] C. Li, J. Wang, H. Liu, F. Guo, X. Xiu, C. Wang, J. Qin, L. Wei, Thermodynamic performance analysis of direct methanol solid oxide fuel cell hybrid power system for ship application, Renew. Energy 230 (2024) 120809.

[12] X. Lv, P. Hong, J. Wen, Y. Ma, C. Spataru, Y. Weng, Highly efficient operation of an innovative SOFC powered all-electric ship system using quick approach for ammonia to hydrogen, Front. Energy 19 (2025) 365–381.

[13] J. Sehested, Four challenges for nickel steam-reforming catalysts, Catal. Today 111 (2006) 103–110.

[14] U.-E.-S. Amjad, C.W.M. Quintero, G. Ercolino, C. Italiano, A. Vita, S. Specchia, Methane steam reforming on the Pt/CeO_2 catalyst: effect of daily start-up and shut-down on long-term stability of the catalyst, Ind. Eng. Chem. Res. 58 (2019) 16395–16406.

[15] M. Gholizadeh, C. Castro, S.M. Fabrega, F. Clarens, A review on thermochemical based biorefinery catalyst development progress, Sustainable, Energy Fuel 7 (2023) 4758–4804.

[16] L. Azancot, L.F. Bobadilla, J.L. Santos, J.M. Córdoba, M.A. Centeno, J.A. Odriozola, Influence of the preparation method in the metal-support interaction and reducibility of Ni-Mg-Al based catalysts for methane steam reforming, Int. J. Hydrog. Energy 44 (2019) 19827–19840.

[17] X. Zhang, K. Yim, J. Kim, D. Wu, S. Ha, Elucidating the promoting role of Mo_2C in methane activation using Ni-xMo_2C/FAU to catalyze methane steam reforming, Appl. Catal. B Environ. 310 (2022) 121250.

[18] E. Dahdah, J. Estephane, C. Gennequin, A. Aboukaïs, E. Abi-Aad, S. Aouad, Zirconia supported nickel catalysts for glycerol steam reforming: effect of zirconia structure on the catalytic performance, Int. J. Hydrog. Energy 45 (2020) 4457–4467.

[19] H. Yang, X. Wang, J. Wang, H. Liu, H. Jin, J. Zhang, G. Li, Y. Tang, C. Ye, High-value utilization of agricultural waste: a study on the catalytic performance and deactivation characteristics of iron-nickel supported biochar-based catalysts in the catalytic cracking of toluene, Energy 323 (2025) 135806.

[20] Y. Guo, L. Zhou, H. Kameyama, Steam reforming reactions over a metal-monolithic anodic alumina-supported Ni catalyst with trace amounts of noble metal, Int. J. Hydrog. Energy 36 (2011) 5321–5333.

[21] Y. Sun, Y. Zhu, T. Xin, X. Li, X. Zhou, G. Bai, W. Chang, R. Zhu, Preparation modification and water resistance optimization of Cu-Mn CO catalyst, Appl. Surf. Sci. 708 (2025) 163768.

[22] L. He, Y. Ren, B. Yue, S.C.E. Tsang, H. He, Tuning metal–support interactions on Ni/Al_2O_3 catalysts to improve catalytic activity and stability for dry reforming of methane, Processes 9 (2021) 706.

[23] J. Horlyck, M. Sara, E.C. Lovell, R. Amal, J. Scott, Effect of metal-support interactions in mixed Co/Al catalysts for dry reforming of methane, ChemCatChem 11 (2019) 3432–3440.

[24] K.S. Park, M. Son, M.-J. Park, D.H. Kim, J.H. Kim, S.H. Park, J.-H. Choi, J.W. Bae, Adjusted interactions of nickel nanoparticles with cobalt-modified $MgAl_2O_4$-SiC for an enhanced catalytic stability during steam reforming of propane, Appl. Catal. A Gen. 549 (2018) 117–133.

[25] G.P. Szijjártó, Z. Pászti, I. Sajó, A. Erdőhelyi, G. Radnóczi, A. Tompos, Nature of the active sites in Ni/$MgAl_2O_4$-based catalysts designed for steam reforming of ethanol, J. Catal. 305 (2013) 290–306.

[26] A. Hadi Abdullah, A.Z. Ab Halim, A.H. Mohamed, M.A. Asshaary Daud, A.H. A. Dabwan, Biogas dry reforming: development of Ni/Na zeolite catalyst using response surface methodology approach with reaction mechanism evaluation, Water Conserv. Manage. 7 (2023) 60–76.

[27] K.S. Park, M.H. Jeong, J.W. Bae, Synergy effects of cobalt oxides on Ni/Co-embedded Al_2O_3 for hydrogen-rich syngas production by steam reforming of propane, Catalysts 10 (2020) 461.

[28] H. Kim, Y.-H. Lee, H. Lee, J.-C. Seo, K. Lee, Effect of Mg contents on catalytic activity and coke formation of mesoporous Ni/Mg-aluminate spinel catalyst for steam methane reforming, Catalysts 10 (2020) 828.

[29] Z. Bian, W. Zhong, Y. Yu, Z. Wang, B. Jiang, S. Kawi, Dry reforming of methane on Ni/mesoporous-Al_2O_3 catalysts: effect of calcination temperature, Int. J. Hydrog. Energy 46 (2021) 31041–31053.

[30] S. Yu, Y. Hu, H. Cui, Z. Cheng, Z. Zhou, Ni-based catalysts supported on $MgAl_2O_4$ with different properties for combined steam and CO_2 reforming of methane, Chem. Eng. Sci. 232 (2021) 116379.

[31] Y. Khani, N. Kamyar, F. Bahadoran, S.S. Lam, S.-H. Jang, Y.-K. Park, MAl_2O_4 (M: Mg, Ni, and Co) as unique support for Ni active metal to form a catalyst for renewable biohydrogen and syngas production from glycerol reforming over a microchannel reactor, Fuel 332 (2023) 126119.

[32] Y. Li, S. Huang, B. Lu, Z. Deng, D. Dong, X. Zhang, S. Wu, X. Deng, The performances of Ni-MgO@γ-Al_2O_3 for steam methane reforming prepared by freeze-drying technology, Int. J. Hydrog. Energy 60 (2024) 729–739.

[33] B.O. Yusuf, M. Umar, E. Kotob, A. Abdulhakam, O.A. Taialla, M.M. Awad, I. Hussain, K.R. Alhooshani, S.A. Ganiyu, Recent advances in bimetallic catalysts for methane steam reforming in hydrogen production: current trends, challenges, and future prospects, Chem. Asian J. 19 (2024) e202300641.

[34] T.S. Moraes, V.S. Bergamaschi, J.C. Ferreira, E.V. Spinacé, Preparation and characterization of high-performance Ni-based core–shell catalyst for ethanol steam reforming, J. Mater. Sci. 57 (2022) 5384–5395.

[35] T.-Y. Kim, J.-H. Lee, S. Jo, J. Kim, J.-H. Woo, R. Dhanusuraman, J.-C. Kim, S.-C. Lee, Improving the stability of Ru-doped Ni-based catalysts for steam methane reforming during daily startup and shutdown operation, Catalysts 13 (2023) 949.

[36] F. Zarei-Jelyani, F. Salahi, M. Farsi, M. Reza Rahimpour, Synthesis and application of Ni-Co bimetallic catalysts supported on hollow sphere Al_2O_3 in steam methane reforming, Fuel 324 (2022) 124785.

[37] F. Salahi, F. Zarei-Jelyani, M. Esmaeilzadeh, M.R. Rahimpour, Investigating the effect of nickel active site position and synthesis method on performance of Ni-La-Al_2O_3 catalyst in the steam reforming of methane: optimization by Box Behnken Design (BBD), J. Energy Inst. 122 (2025) 102183.

[38] S.B. Karakache, M. Rouabah, R. Gosselin, N. Abatzoglou, I.E. Achouri, Experimental study and statistical analysis of hydrogen yield in methane steam reforming over a hydroxyapatite-supported nickel catalyst, Catal. Today 456 (2025) 115322.

[39] M. Meshksar, M. Farsi, M.R. Rahimpour, Effect of Ni active site position and synthesis route on activity, stability, and morphology of Ce promoted Ni/Al_2O_3 catalyst for clean H_2 production, J. Environ. Chem. Eng. 10 (2022) 108471.

[40] B. Han, F. Wang, L. Zhang, Y. Wang, W. Fan, L. Xu, H. Yu, Z. Li, Syngas production from methane steam reforming and dry reforming reactions over sintering-resistant Ni@SiO_2 catalyst, Res. Chem. Intermed. 46 (2019) 1735–1748.

[41] Q. Lu, Y. Hou, S.R. Laraib, O. Khalifa, K. Li, W.-L. Xie, M.-S. Cui, Y.-P. Yang, Electro-catalytic steam reforming of methane over Ni-CeO_2/γ-Al_2O_3-MgO catalyst, Fuel Process. Technol. 192 (2019) 57–64.

[42] L. Zhou, Y. Guo, H. Kameyama, J.-M. Basset, An anodic alumina supported Ni–Pt bimetallic plate-type catalysts for multi-reforming of methane, kerosene and ethanol, Int. J. Hydrog. Energy 39 (2014) 7291–7305.

[43] L. Xu, J. Zhang, F. Wang, K. Yuan, L. Wang, K. Wu, G. Xu, W. Chen, One-step synthesis of ordered mesoporous $CoAl_2O_4$ spinel-based metal oxides for CO_2 reforming of CH_4, RSC Adv. 5 (2015) 48256–48268.

[44] P.V. Ponugoti, P. Pathmanathan, J. Rapolu, A. Gomathi, V.M. Janardhanan, On the stability of Ni/γ-Al_2O_3 catalyst and the effect of H_2O and O_2 during biogas reforming, Appl. Catal. A Gen. 651 (2023) 119033.

[45] S.I. Uskov, D.I. Potemkin, P.V. Snytnikov, V.D. Belyaev, O.A. Bulavchenko, P. A. Simonov, V.A. Sobyanin, Ni-MO_x-Al_2O_3 (M = Mg, Cr, Ce) catalysts prepared by Pechini technique for low temperature steam reforming of light hydrocarbons into methane-rich gas, Mater. Lett. 221 (2018) 18–21.

[46] A.H. Braga, D.C. de Oliveira, A.R. Taschin, J.B.O. Santos, J.M.R. Gallo, J.M. C. Bueno, Steam reforming of ethanol using Ni-Co catalysts supported on $MgAl_2O_4$: structural study and catalytic properties at different temperatures, ACS Catal. 11 (2021) 2047–2061.

[47] C. Ruocco, V. Palma, A. Ricca, Experimental and kinetic study of oxidative steam reforming of ethanol over fresh and spent bimetallic catalysts, Chem. Eng. J. 377 (2019) 119778.

[48] N.A. Abd Ghani, A. Azapour, A.F.A. Syed Muhammad, B. Abdullah, Dry reforming of methane for hydrogen production over Ni Co catalysts: effect of Nb Zr promoters, Int. J. Hydrog. Energy 44 (2019) 20881–20888.

[49] L. Wang, D. Li, M. Koike, H. Watanabe, Y. Xu, Y. Nakagawa, K. Tomishige, Catalytic performance and characterization of Ni-Co catalysts for the steam reforming of biomass tar to synthesis gas, Fuel 112 (2013) 654–661.
[50] X.L. Li, J. Bao, Z. Shadike, Q.C. Wang, X.Q. Yang, Y.N. Zhou, D. Sun, F. Fang, Stabilizing transition metal vacancy induced oxygen redox by Co^{2+}/Co^{3+} redox and sodium-site doping for layered cathode materials, Angew. Chem. Int. Ed. 60 (2021) 22026–22034.
[51] A.H. Fakeeha, A.A. Ibrahim, W.U. Khan, A.E. Abasaeed, A.S. Al-Fatesh, Hydrogen production by catalytic methane decomposition over Ni, Co, and Ni-Co/Al_2O_3 catalyst, Pet. Sci. Technol. 34 (2016) 1617–1623.
[52] E. Tezel, H.E. Figen, S.Z. Baykara, Hydrogen production by methane decomposition using bimetallic Ni-Fe catalysts, Int. J. Hydrog. Energy 44 (2019) 9930–9940.
[53] L. Alalga, A. Benamar, M. Trari, Hydrogen production via methane decomposition over nickel supported on synthesized ZSM-5/MCM-41 zeolite composite material, Int. J. Hydrog. Energy 46 (2021) 28501–28512.
[54] I. Alshibane, S. Laassiri, J.L. Rico, J.S.J. Hargreaves, Methane cracking over cobalt molybdenum carbides, Catal. Lett. 148 (2018) 1643–1650.
[55] M. Pudukudy, Z. Yaakob, Q. Jia, M. Sobri Takriff, Catalytic decomposition of undiluted methane into hydrogen and carbon nanotubes over Pt promoted Ni/CeO_2 catalysts, New J. Chem. 42 (2018) 14843–14856.
[56] M.V. Chudakova, M.V. Popov, P.A. Korovchenko, E.O. Pentsak, A.R. Latypova, P. B. Kurmashov, A.A. Pimenov, E.A. Tsilimbaeva, I.S. Levin, A.G. Bannov, A. V. Kleymenov, Effect of potassium in catalysts obtained by the solution combustion synthesis for co-production of hydrogen and carbon nanofibers by catalytic decomposition of methane, Chem. Eng. Sci. 284 (2024) 119408.
[57] R. Alizadeh, E. Jamshidi, H. Ale Ebrahim, Kinetic study of nickel oxide reduction by methane, Chem. Eng. Technol. 30 (2007) 1123–1128.
[58] M.C. Altay, S. Eroglu, Non-isothermal reduction behavior of NiO in undiluted Ar and CH_4 atmospheres, Int. J. Miner. Process. 149 (2016) 50–55.
[59] M.-J. Kim, S. Joo Park, K. Duk Kim, W. Kim, S. Chan Nam, K. Seok Go, S. Goo Jeon, Fabrication of carbon nanotube with high purity and crystallinity by methane decomposition over ceria-supported catalysts, J. Ind. Eng. Chem. 119 (2023) 315–326.
[60] A.E. Awadallah, A.A. Aboul-Enein, M.A. Deyab, M.A. Azab, A.M. Haggar, Impact of Cr doping on the performance of Ni/Al_2O_3 catalyst through methane decomposition into CO_x-free hydrogen and carbon nanomaterials, Chem. Eng. Res. Des. 186 (2022) 701–712.
[61] J.-R. Youn, M.-J. Kim, K.C. Kim, M. Kim, T. Jung, K.-S. Go, S.G. Jeon, W. Kim, Highly efficient Co-added Ni/CeO_2 catalyst for co-production of hydrogen and carbon nanotubes by methane decomposition, Fuel Process. Technol. 263 (2024) 108130.
[62] F.-X. Chiron, G.S. Patience, Steam carbon gasification of a nickel based oxygen carrier, Fuel 90 (2011) 2461–2466.